Research Article

Journal of PeptideScience

Received: 12 January 2009 Revised: 10 March 2009 Accepted: 14 May 2009 Published online in Wiley Interscience:

(www.interscience.com) DOI 10.1002/psc.1152

Antimicrobial peptide interactions with silica bead supported bilayers and *E. coli*: buforin II, magainin II, and arenicin‡

Ryan W. Davis,[a]* Dulce C. Arango,[b] Howland D. T. Jones,[c] Mark H. Van Benthem,[d] David M. Haaland,[c] Susan M. Brozik[b] and Michael B. Sinclair[a]

Using the unique quantitative capabilities of hyperspectral confocal microscopy combined with multivariate curve resolution, a comparative approach was employed to gain a deeper understanding of the different types of interactions of antimicrobial peptides (AMPs) with biological membranes and cellular compartments. This approach allowed direct comparison of the dynamics and local effects of buforin II, magainin II, and arenicin with nanoporous silica bead supported bilayers and living *E. coli*. Correlating between experiments and comparing these responses have yielded several important discoveries for pursuing the underlying biophysics of bacteriocidal specificity and the connection between structure and function in various cellular environments. First, a novel fluorescence method for direct comparison of a model and living system is demonstrated by utilizing the membrane partitioning and environmental sensitivity of propidium iodide. Second, measurements are presented comparing the temporal dynamics and local equilibrium concentrations of the different antimicrobial agents in the membrane and internal matrix of the described systems. Finally, we discuss how the data lead to a deeper understanding of the roles of membrane penetration and permeabilization in the action of these AMPs. Copyright © 2009 European Peptide Society and John Wiley & Sons, Ltd.

Supporting information may be found in the online version of this article

Keywords: antimicrobial peptides; biomimetic systems; spectral imaging; supported bilayers; mesoporous silica; multivariate curve resolution; FRET; buforin II; magainin II; arenicin; nanoscale encapsulation; bio-materials interfaces; nanoporous containment

Introduction

Widespread resistance of bacterial pathogens to existing antibiotics has resulted in increased interest in non-traditional microbial inhibitors and antimicrobial peptides (AMPs) [1–4]. AMPs are generally short chain, polycationic and amphiphilic peptides (~15–30 residues), which interact with microbes in various ways. To date, some elucidated mechanisms of antimicrobial function include inhibition of cell wall formation, disruption of membrane potential by pore formation or carpet model-like disintegration, alteration of gene expression, and inhibition of nuclease activity [3–5]. In general, AMPs are stable over a wide range of pH values and have broad spectrum activity *in vivo* as well as synergy with other antimicrobial agents [6–9]. Although this growing class of peptides presents an exciting model for combating infection and pathogenic resistance, several challenges must be overcome to produce safe and effective AMP-based therapeutic agents. Gaining a detailed understanding of the chemical basis for the observed cytotoxic specificity and the connection between the structure and function of these peptides in myriad cellular environments are paramount among these challenges. In order to effectively address these issues, new methods and experimental platforms are needed to characterize AMP interactions with different microscopic physiological structures. In this work, two well-studied examples, magainin II and buforin II, as well as a recently discovered example, arenicin, are probed for activity in model silica bead supported bilayers (SBSBs) and *E. coli*. By comparing the response of these markedly distinct antimicrobial agents in the reductionist and natural system, a more cohesive understanding of the chemical partitioning, structural variation, and biophysical mechanism of these agents can be used for designing next generation therapies.

* *Correspondence to: Ryan W. Davis, Electronic and Nanostructured Materials, Sandia National Laboratories, Albuquerque, NM, 87185–0892, USA. E-mail: rwdavis@sandia.gov*

a *Electronic and Nanostructured Materials, Sandia National Laboratories, Albuquerque, NM, 87185-0892, USA*

b *Biosensors and Nanomaterials, Sandia National Laboratories, Albuquerque, NM, 87185-0892, USA*

c *Biomolecular Analysis and Imaging, Sandia National Laboratories, Albuquerque, NM, 87185-0892, USA*

d *Materials Characterization, Sandia National Laboratories, Albuquerque, NM, 87185-0892, USA*

Antimicrobial Peptides

Recent computer-aided efforts for generation of pharmaceutical lead compounds have yielded a generalized set of 890 previously described AMPs [10], and the prospects are good for this number to increase significantly in the near future. In spite of the large numbers of potential AMP drug candidates, structural analysis suggests that four major classes including β-sheet, α-helical, loop, and extended peptides dominate the bulk of known AMP sequences [11]. In this work, we focused on three AMPs with variable structure and function: magainin II, buforin II, and arenicin.

Magainin II, a 23 amino acid amphiphilic and cationic peptide isolated from the skin of the African clawed frog, *Xenopus laevis*, is believed to preferentially bind to anionic membranes, generating a pore that dissipates ionic gradients, thus killing the cell [12–14]. Following binding to the membrane, the commonly accepted mechanism of antimicrobial activity involves insertion and aggregation of the alpha helix structure to form a dynamic peptide–lipid supermolecular pore in gram-negative bacterial membranes. This toroidal membrane spanning pore is unique in that the resulting peptide pentamer integrates phospholipids curved perpendicular to the plane of the membrane, thus lining the pore with hydrophilic residues [14,15].

Buforin II, a 21 amino acid cationic peptide expressed by amphibians, is believed to penetrate the cell membrane without permeabilization and kill the cell instead by disrupting RNase/DNase activity [16–19]. In a hydrophobic medium, the protein's secondary structure includes an N-terminal random coil region, an extended helical region, a proline hinge, and a C-terminal alpha helical region [20,21]. Antimicrobial activity in this structure is dictated by several factors to varying degrees. The most pronounced change occurs under disruption of the C-terminal region in which all antimicrobial activity is removed. In deletion of the N-terminal region, an increase in antimicrobial activity is observed; however, truncation of this region results in decreased overall activity. Finally, substitution of the proline hinge with a leucine residue results in loss of the peptide's ability to penetrate the membrane, thus eliminating all antimicrobial activity [21].

Arenicin, a 21 amino acid cationic peptide discovered in 2004 in coelomocytes of the lugworm *Arenicola marina* [22], has been found to be toxic to both gram-negative and gram-positive bacteria in low concentrations. Structurally, this peptide contains a disulfide bond that results in the formation of an 18 residue loop unique among AMPs. Several recent studies show that one potential mechanism of action involves cell permeation resembling barrel-stave pore formation, although additional mechanisms have also been suggested [23–25].

Materials and Methods

Bacterial Culture

E. coli cultures were prepared by streaking the K-12 ATCC 10 798 strain from glycerol stock onto a Luria-Bertaini (LB) agar plate. After 24 h of incubation at 37 °C, single colonies were inoculated in 1–5 ml LB media and incubated in a S-500 orbital shaker (VWR) on setting 4 at 37 °C for 16 h. Finally, optical density measurements were performed by monitoring the absorbance at 640 nm to confirm log-phase growth.

Liposome Preparation

Fluorescent and non-fluorescent phospholipids were purchased from Invitrogen Corp., Carlsbad, CA, USA and Avanti Polar Lipids, respectively (Lissamine™ rhodamine 1,2-dihexadecanoyl-sn-glycero-3-phosphoethoanoamine, triethylammonium salt: Rhod-DHPE; *E. coli* L-α-phosphatidylethanolamine: PE; *E. coli* L-α-phosphatidylglycerol: PG). Before use, each was dissolved in chloroform and stored at −80 °C. *E. coli* lipopolysaccheride (LPS) was purchased from Sigma-Aldrich, St Louis, MO, USA and dissolved in methanol prior to use. For the assays described below, equal molar ratios of PE and PG were combined in a round bottom flask. Where fluorescent phospholipids were desired, Rhod-DHPE was also added as a chloroform solution to achieve 1% mol/mol fluorescent component. In assays meant to mimic the gram-negative outer membrane, liposomes incorporating LPS were produced by adding this component to the other lipids as a methanol solution at a relative concentration of 10% mol/mol. Once all of the desired components had been combined, the solvent was removed by drying under a stream of nitrogen. The resulting phospholipid cakes were then further dried under vacuum for a minimum of 20 min. The phospholipid cake was then reconstituted in 1 × phosphate buffered saline (PBS) containing 10 mM $CaCl_2$ (pH 7.2) to achieve a total PE/PG concentration of 2.4 mM. Once the lipid cake was fully dissolved, the resulting liposome suspension was transferred to a Falcon® tube and subject to sonication using a Branson 250 Ultrasonicator (microtip setting = 6, duty cycle 20%) for 10 min at 4 °C, at which time turbidity was no longer observed.

SBSB Self-Assembly

Monodispersed nanoporous silica microspheres (Nucleosil, 10 µm in diameter, 10 nm pores, GFS Chemicals, Inc., Powell, OH, USA) were employed as the substrate for SBSB self-assembly. Silica beads were weighed and treated in a 4% peroxide/4% ammonium hydroxide solution at 80–90 °C for 10 min. The beads were then centrifuged and washed three times with Nanopure® water and suspended in 1 × PBS containing 10 mM $CaCl_2$ (pH 7.2). The desired number of beads was then pipetted with stirring from a stock suspension (1.25×10^8 beads/ml) and the supernatant removed. Freshly prepared PE/PG liposome solution was then added to the suspension and vortexed on the lowest setting for 45 min to promote supported bilayer formation. The suspension was then allowed to sit undisturbed for 5 min. The SBSB samples were then centrifuged and washed with PBS to remove free phospholipids in solution. Fluorescence titration measurements of SBSBs containing 1% mol/mol Rhod-DHPE were used to determine the number of washes necessary for removal of phospoholipids unincorporated into the supported bilayer. In parallel with these titration measurements, bilayer stacking was probed by fluorescence intensity measurements on samples containing 1% mol/mol Rhod-DHPE before and following 20 min exposure to 0.3 M KI quencher. In each of these assays, fluorescence intensity values were attainted by integrating over a 10 nm spectral region centered at 610 nm with an excitation wavelength of 535 ± 5 nm.

Fluorescence Labeling

Covalent fluorescent conjugation of fluorescein isothiocyanate (FITC) to the N-terminal region of these AMPs was performed by two external providers, GenScript, Piscataway, NJ, USA and BioSynthesis, Inc., Lewisville, TX, USA. Optical density measurements were performed on AMP exposed (0.1 mg/ml) log-phase *E.*

Journal of PeptideScience

coli grown in LB medium by monitoring the absorbance at 640 nm. Compared with controls, all unlabeled AMPs showed bacterial kill rates of >90%, whereas labeled AMPs killed between 75 and 89% of the cells. In cases where the activity of the labeled AMP differed between the two providers' samples, the sample with the greater ability to kill *E. coli* was chosen for future use. In order to monitor the lysis statistics of *E. coli* following exposure to the different AMPs in hyperspectral imaging applications, propidium iodide (PI) was added to the culture at a rate of 0.125 mg/ml.

Several methods of membrane labeling were performed and compared for investigations of AMP interactions with SBSBs and the cell envelopes of *E. coli*. The first method, which was previously demonstrated for labeling *E. coli* membrane proteins nonspecifically [26], was direct conjugation of an amine-reactive Alexafluor 594, succinimydl ester fluorescent label (Invitrogen, Inc.). This was performed by combining log-phase *E. coli* in 1× PBS (pH 8.5) and the fluorescent probe (2.5 mg/ml), followed by incubation at 4 °C for 16 h, purification via centrifugation, and hyperspectral fluorescence imaging. The second method sought to introduce a Rhod-DHPE phospholipid label into *E. coli* membranes by way of liposome or micelle exchange. For liposome exchange, Rhod-DHPE containing PE/PG liposomes were combined with log-phase *E. coli* at ratios corresponding to phospholipid concentrations between 10 and 5 mM. For micelle exchange, dodecyl nonaoxyethylene ether (C12E9) [Fluka, critical micelle concentration (CMC) = 0.9 mM] and 1% mol/mol Rhod-DHPE were co-dissolved in 1× PBS and combined with log-phase *E. coli* at ratios corresponding C12E9 concentrations between 0.1 and 10× (CMC). *E. coli* suspensions containing fluorescent liposomes or micelles were then subjected to hourly optical density measurements by monitoring the absorbance at 640 nm, and hyperspectral fluorescence imaging to determine the degree of localization of Rhod-DHPE in the sample. The final method sought to introduce an *E. coli* membrane label using a fluorescent conjugate of ethylenediaminetetraacetic acid (EDTA), Rhod-5N (Invitrogen, Inc.). For this method, Rhod-5N was added to log-phase *E. coli* at concentrations ranging between 1 and 10 μM, after which the cells were subjected to optical density measurements and hyperspectral fluorescence imaging as performed above.

Comparison of AMP predicated rupture of SBSBs was performed by a Tb^{3+} release assay. This was achieved by adding 10 mM $TbCl_3 \cdot (H_2O)_6$ (99.999%, Sigma-Aldrich) to the internal SBSB buffer solution prior to PE/PG liposome exposure and washing, and followed by addition of dipicholinic acid to adjust the external buffer concentration to 10 mM. After 5 min of equilibration, 0.1 mg/ml AMP was added to the SBSB sample, and fluorescence emission measurements were taken by integrating over a 10 nm spectral band centered at 545 nm (λ_{ex} = 275 nm) at regular intervals over 1 h.

Hyperspectral Fluorescence Imaging and Multivariate Analysis

Observation of the dynamics of AMPs with SBSBs and living bacteria required both standard microscopic techniques and flow cell control. The flow cell constructed for these experiments employed aluminum housing with a center perforation through which buffer was routed from the top of the sample through a 1 μm pore size polycarbonate filter (Whatman, Inc., Sanford, ME, USA). Flow was controlled using dedicated syringe pumps (Harvard Apparatus, Inc., Holliston, MA, USA) for buffer and analyte delivery, and the total flow cell volume was calibrated to 1 ml. Cellular immobilization was accomplished using poly-l-lysine coated coverslips (BD Biosciences, San Jose, CA, USA).

High spectral resolution time series imaging and confocal sectioning was performed using Sandia National Laboratories' unique 3D hyperspectral confocal fluorescence imaging capabilities [27]. In this system, a 488 nm continuous wave laser is used for raster illumination covering a 25 × 25 μm field of view using a 60×, 1.4 NA Plan Apo objective (Nikon Instruments, Melville, NY, USA), corresponding to an excitation power of ~5 kW/cm^2 at the sample. At each imaging voxel, a spectrum is collected with resolution of 1–3 nm over a 500–800 nm wavelength region at a rate of 4160 spectra/s. This spectral imaging rate is achieved using a high performance galvanometer (Cambridge Tech, Inc., Cambridge, MA, USA) synchronized with a push-broom custom readout from an EMCCD camera (Andor, Inc., Belfast, IRE, UK), with computer synchronization using an object-oriented graphical interface. Spatial resolution under these conditions is 235 nm in the XY plane (2–3 pixels), and ~600 nm in the Z direction. Emission wavelength calibration was performed using a hollow-cathode Kr^+ lamp, and dark images were collected at regular intervals during data collection to correct for instrument offset and background signals.

Spectral imaging data provide a two-way data set for multivariate curve resolution (MCR) analysis [28]. MCR uses the heterogeneous spatial and spectral information of two-way data iteratively to extract the least-squares pure-component spectra and the associated relative quantitative concentrations from hyperspectral images. The theory behind MCR algorithms are not within the scope of this paper and are described elsewhere [29–33]. In this work, MCR was implemented using a nonnegative constrained alternating least-squares algorithm [30]. Nonnegativity constraints were employed for the pure spectral components and the corresponding concentrations, reflecting the lack of negative spectral features in real fluorescence data. The MCR software consists of custom C++ code (AXSIA) that is called by a custom Matlab GUI program (runAXSIA). AXSIA [34] performs the MCR analyses, whereas runAXSIA is used to preprocess the spectral image data, set up the MCR parameters, and display the results from the MCR analyses (spectral components, images, and diagnostics). In order to deal with several noise sources inherent to hyperspectral image collection (Poisson distributed, structured, and read noise) which complicate the ability to extract the pure-component spectra and their associated concentrations, rigorous characterization of the instrument noise has been performed and the data weighted appropriately [35,36].

Results

SBSB Characterization

Figure 1 illustrates the self-assembly of SBSBs on nanoporous silica microspheres. Confocal Z-sectioning was used to verify the formation of supported bilayers via emission from the fluorescent membrane component, Rhod-DHPE. It was found, however, that PE/PG liposomes do not form on clean silica microspheres without the addition of a cationic counter-ion, which in this case was Ca^{2+}. Alteration of the overall concentration of Ca^{2+} concentration in the liposome buffer resulted in highly homogenous SBSBs over a concentration range restricted to ~2–10 mM. Following successful self-assembly, characterization of the resulting supported bilayers was performed by two bulk fluorescence assays in addition to spectral fluorescence imaging. The first of these assays monitored the fluorescence intensity of Rhod-DHPE doped PE/PG SBSBs

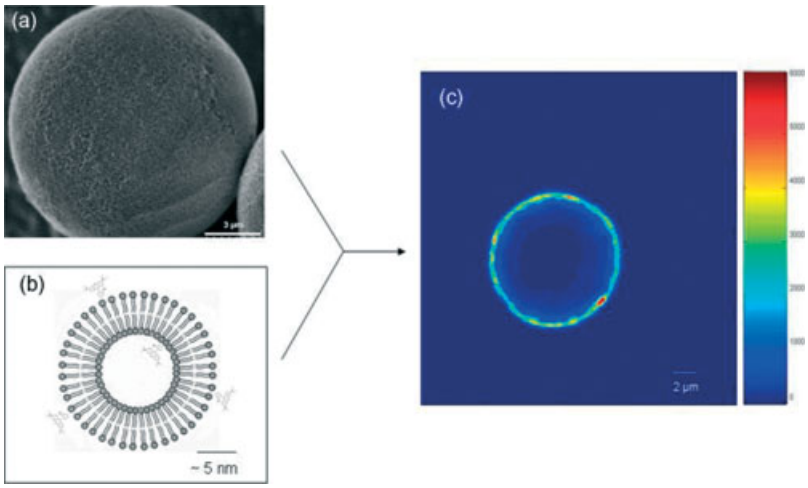

Figure 1. Formation of a SBSB. (a) Scanning electron microscope image of a 10 μm in diameter nanoporous silica microsphere, combined with (b) fluorescently labeled unilamellar PE/PG liposome solution produces (c) supported bilayer encapsulating a nanoporous silica microsphere following 6× centrifuge/buffer wash cycles, as seen in the hemispherical confocal fluorescence section of the isolated Rhod-DHPE (1% mol/mol) MCR emission component with color-coded intensities.

between subsequent centrifuge/wash cycles to characterize the degree of loosely adsorbed bilayers. In this assay, a large decrease in SBSB fluorescence is observed within the first three to four wash cycles, and single supported bilayer coverage is achieved after six wash cycles. The ratio of the starting to final fluorescence intensity is ~6×, suggesting the initial presence of a multilamellar stack of supported bilayers. The second fluorescence assay used for characterization of the SBSBs used iodide quenching of bilayer integrated Rhod-DHPE to establish the percentage of the membrane surface accessible to the external solvent. Control studies employing non-phospholipid conjugated Rhodamine dye in solution exhibit quenching rates in excess of 97% in the presence of 0.3 M KI. In the experimental system, decay of the fluorescence intensity with increasing washes was observed, finally achieving ~45% compared with controls following six wash cycles. Assuming a random orientation of quenchable Rhod-DHPE in the SBSBs, ~50% quenching would be expected in a unilamellar bilayer. Combining the observations from these two assays and the spectral imaging data suggest that SBSB self-assembly with anionic bilayers and divalent cationic counter-ions initially produces a highly stacked multilamellar membrane, which can be delaminated to a single unilamellar bilayer by repeated centrifuge/wash cycles with low ionic strength buffer.

Fluorescent Membrane Labeling

Several methods to produce a stable and membrane selective fluorescence label for *E. coli* were attempted and the results are depicted in Figure 2. The conventional covalent membrane attachment protocol of Bradburne *et al*. [26] resulted in weakly emitting membrane-localized fluorescence that dissipated after ~15 min in a flow cell running at 0.1 ml/min, as well as general altered morphology of the *E. coli* characterized by elongation and swelling. Exchange between fluorescent amphiphilic lipid phases and *E. coli* membranes was similarly unsatisfactory; in the case of liposomes, no fluorescence exchange was observed, and in the case of C12E9 micelles, all concentrations proved to be destructive to *E. coli*. Additionally, introduction of a fluorescent analogue of EDTA, Rhod-5N, displayed inhomogenous labeling at low concentrations (1 μM) and cell lysis at concentrations exceeding 10 μM.

The solution that was ultimately employed to alleviate the observed membrane labeling issues came as an unexpected observation from spectral imaging of *E. coli* in the presence of the cell lysis indicator, PI [37]. As shown in Figure 3, this intensity-based indicator undergoes a fluorescence red-shift of 10 nm at the membrane edge of the bacterium. MCR analysis of images collected in this manner show the presence of two distinct spectral components with high spatial orthogonality (in addition to a cellular autofluorescence component). The fact that the red-shifted PI fluorescent component corresponds to 2–3 pixels in width suggests that this component correlates to a diffraction limited (≤235 nm) spatial region coincident with the expected membrane location. Fluorescence spectra of control experiments employing PE/PG liposomes show a similar fluorescence shift of PI only when LPS is included as a constituent, suggesting that this red-shifted component corresponds to partitioning of PI in the gram-negative outer membrane of *E. coli*. In order to test the specificity of this effect, an identical concentration of PI was added to a culture of the gram-positive bacterium, *Micrococcus lysodeikticus,* and no similar red-shifted PI fluorescent component was observed, supporting the hypothesis that PI can be employed as a specific indicator for the gram-negative outer membrane. This property of PI thus adds to its single experiment functionality, reporting simultaneously on the lysis state of the cell and the localization of an important membrane component. Building on this result, MCR spectral separation of the red-shifted PI component was selected for subsequent equilibrium and fluorescence resonant energy transfer (FRET) studies involving fluorescent AMP conjugates and the *E. coli* bacterial membrane.

Comparative Local AMP Concentrations

Measuring the relative equilibria of AMP partitioning in SBSBs and *E. coli* was performed in order to gain a deeper understanding of the physiological localization of bacteriocidal action (Figure 4). This was achieved by exposing the system under study to a functionally active concentration of fluorescent AMP (0.1 mg/ml) in the presence of membrane specific fluorescent probes and

Journal of PeptideScience

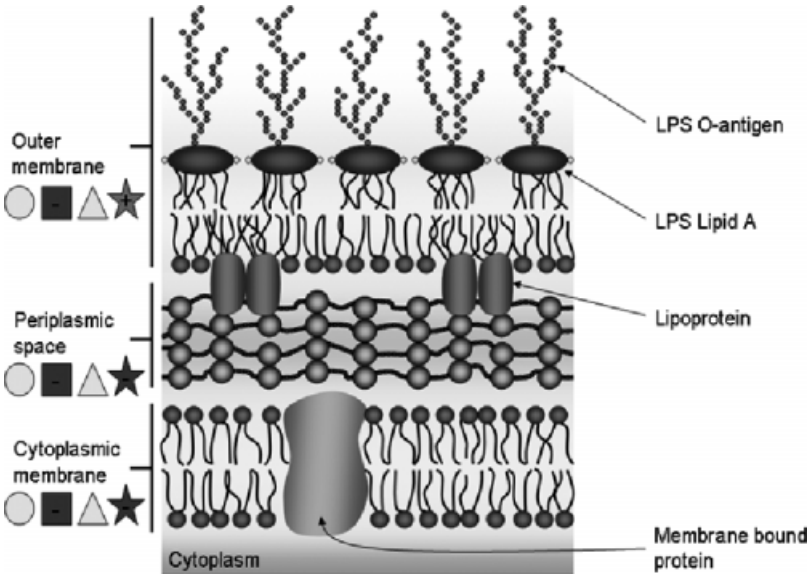

Figure 2. *E. coli* membrane labeling. The gram-negative cellular envelope is composed of three primary biochemical regions: the outer membrane, the periplasmic space, and the cytoplasmic membrane. The results of four fluorescence labeling schemes are depicted below the label of each region: 1, covalent conjugation of fluorophores via succinimidyl ester reactions with amino groups on membrane-bound proteins (circle); 2, micelle- or liposome-mediated exchange of fluorescent phospholipids (square); 3, EDTA-modified fluorophore for metal binding site conjugation (triangle); 4, PI chemical partitioning (star). Labeling schemes categorized as producing no fluorescence were designated with a minus sign ('−'), those producing region-specific fluorescence were designated with a plus sign ('+'), and those producing some detectable fluorescence, but with ambiguous region specificity were designated as blank (' ').

autofluorescence, followed by imaging and spectral separation with MCR. This method allows quantification of the local relative concentrations by spatially demarking the membrane, internal matrix, and external solution, and eliminates spectral cross talk intrinsic to multilabel imaging experiments with commercial filter-based microscopes.

A comparison of the relative AMP concentrations between SBSBs and *E. coli* is seen in Figure 3. Close trend similarities are apparent for the two membrane localizations, but there are considerable differences for the internal matrix. These data suggest that although SBSBs seem to mimic the bulk of the important interactions of AMPs with the gram-negative cellular envelope, the silica subsurface poses a significant perturbation to the whole cell partitioning of buforin II and arenicin. This effect is hypothesized to result from the combination of the significant anionic charge of the silica matrix and the AMPs' polycationic nature, although this is not consistent among all of the AMPs. Large error bars in the arenicin results were attributed to the tendency of this AMP to form heterogeneous aggregation states in these systems.

Membrane Penetration and Permeabilization

Perhaps the most dominant of the hypothesized mechanisms of bacteriocidal activity of AMPs is the ability to selectively permeabilize or otherwise disrupt microbial membranes [38–41]. In general, membrane disruption is exemplified by the membrane solubilizing properties of detergent micelles, which is broadly employed throughout the world for sanitation purposes [42]. Other methods for disrupting microbial membranes include electrostatic permeation via metal binding at elevated concentrations (e.g. Ca^{2+}) and EDTA chelation. Thus, the chemical structure of a specific and highly effective AMP may combine these properties to varying degrees.

AMP predicated ion release from SBSBs

As a basis for comparison to spectral imaging data, SBSBs were used for ensemble lanthanide release assays to establish the membrane disruptive properties of each AMP. In this assay, terbium (III) ion was introduced and encapsulated by the supported bilayer in the nanoporous silica matrix. The fluorescence emission intensity of the external solution was measured at 545 nm ($\lambda_{ex} = 275$ nm) periodically to monitor chelation of released Tb^{3+} by dipicolinic acid [43]. Using a standard calibration, Tb^{3+} release was quantified and correlated to AMP exposure. In these experiments, several differences were noted among the AMPs. First, Buforin II resulted in slight Tb^{3+} extrusion, reaching $9 \pm 7\%$ greater than controls after 1 h. Magainin II showed a measured release of Tb^{3+}, finally reaching $48 \pm 10\%$ greater than controls after 1 h. Finally, arenicin demonstrated high extrusion of Tb^{3+} from the bacterial model supported bilayer system which reached $66 \pm 11\%$ greater than controls over the course of 1 h.

AMP–membrane binding and cell lysis

The correlation of permeabilization of the bacterial cell envelope and the localization of magainin II, buforin II, and arenicin were studied via a combination of two time-dependent spectral imaging assays. The first assay employed PI to measure cell lysis statistics and is summarized in Figure 5. The second assay tracing FRET ratios between the AMPs and the fluorescently labeled membranes for monitoring binding dynamics of the AMP to the membrane is summarized in Figure 6. The FRET results were then compared between SBSBs and those from *E. coli*.

Cell lysis statistics were measured by exposing *E.coli* in a flow cell containing 0.125 mg/ml PI to a 0.1 mg/ml pulse of fluorescently labeled AMP solution. The ratio of cells exhibiting $\geq 3\times$ PI fluorescence intensity relative to the average intensity of all other cells collected during the time point was designated as

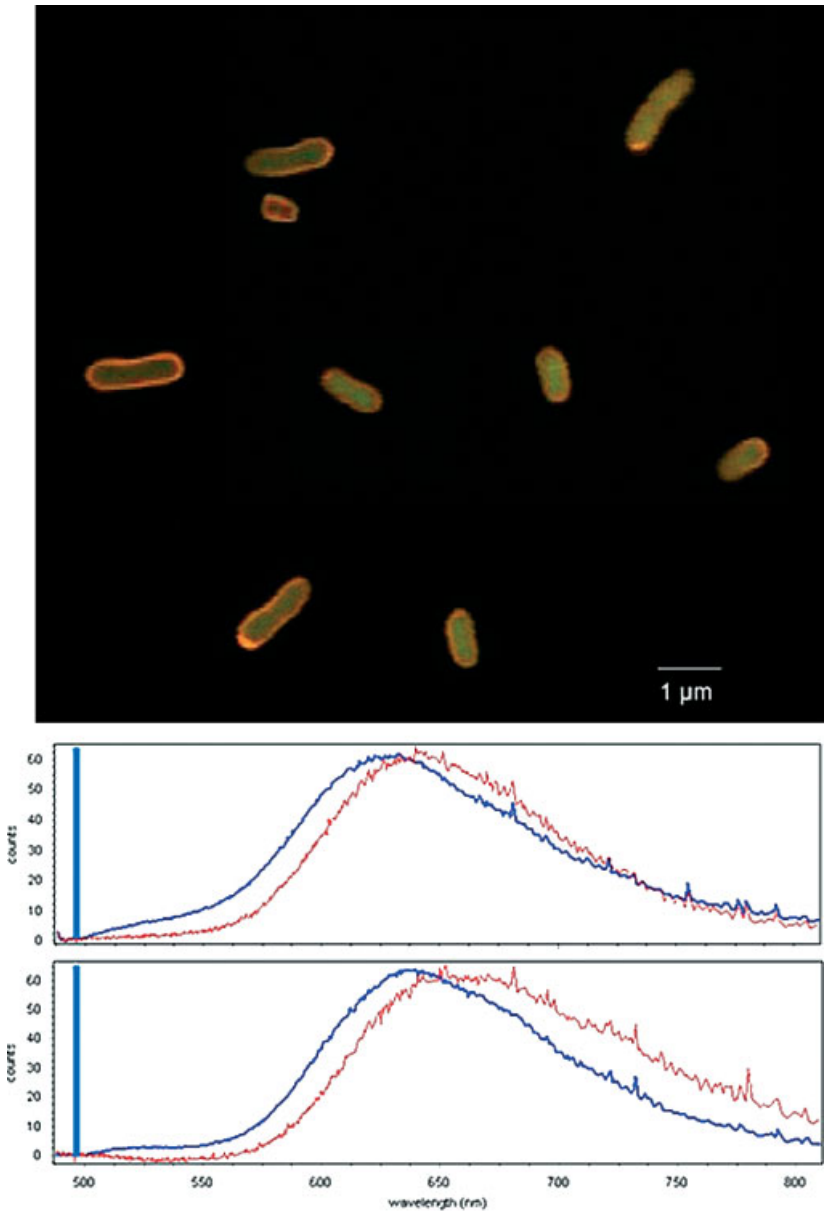

Figure 3. Outer membrane partitioning of PI. Top: False color confocal section generated from MCR fluorescence data showing the red-shifted PI component in the *E. coli* outer membrane. Middle: Bulk fluorescence spectra of PI in PE/PG liposomes (blue-shifted) and PI in PE/PG liposomes containing 10% mol/mol *E. coli* LPS (red-shifted). Bottom: MCR spectra of membrane-localized PI (red-shifted) and internal matrix-localized PI (blue-shifted). The additional vertical line in the spectral plots indicates the spectral location of the 488 nm laser excitation wavelength.

the percent lysed [37]. The average number of cells per time point was 64 ± 9, and the total exposure time was 1.5 h. Compared with controls, buforin II showed no significant increase in lysis of *E. coli*, which is consistent with previous reports [16–19] of the direct effect of buforin II on the bacterial envelope. However, it is important to note that transcription-mediated lysis may be inhibited by competitive binding between PI and buforin II to DNA targets. Magainin II exhibited a 6% increase versus controls within 3 min after exposure, followed by a linear increase with a baseline subtracted slope fitted to +0.14% lysis events per minute ($R^2 = 0.96$). In the case of arenicin, the statistical rate of lysis only slightly exceeded controls that were not exposed to AMP. However, subsequent analysis of the subpopulation of cells exhibiting punctuate distributions of AMP on the cellular envelope yielded a factor of ~3× increase in lysis events compared controls over the course of the assay. These punctuate distributions of arenicin suggest aggregation of this AMP that is coincident with membrane binding and cell lysis.

FRET, a powerful assay in fluorescence microscopy for monitoring binding between biological molecular structures, was implemented by ratiometric comparison of the emission of the AMP donor spectral component (FITC) to the emission of the membrane acceptor spectral component. In both SBSBs, where the acceptor was Rhod-DHPE, and *E. coli*, where the acceptor was the membrane component of PI, the ratio of the acceptor to donor intensity should increase approximately linearly when these two components are within ~1 and 5 nm of one another, according to a Förster-type process [44].

Time series FRET experiments were performed on SBSBs in a flow cell by first flowing buffer for 1 min, then introducing a

Journal of PeptideScience

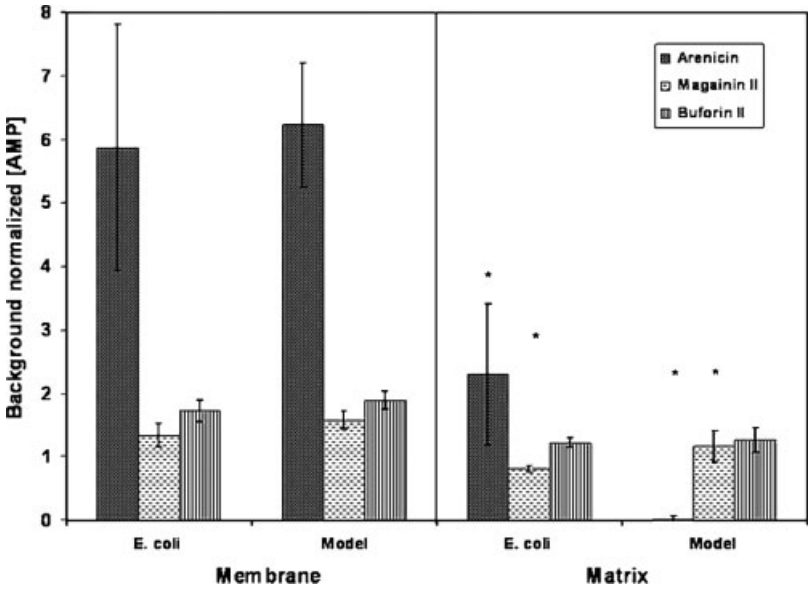

Figure 4. Relative equilibrium concentrations of each AMP in the membrane and internal matrix of SBSBs (model) and *E. coli* following 15 min exposure to 0.3 mg/ml of the specified AMP. The intensities shown are averages over pixel masks and normalized as a multiple of the background AMP intensity. For SBSBs, the membrane and internal matrix data were accumulated from 1310 and 2127 MCR pixels, respectively. For *E. coli*, the membrane and internal matrix data were accumulated from 364 and 283 MCR pixels, respectively. Error bars represent one standard deviation of averaged data. Stars represent data showing statistically significant differences between the *E. coli* and SBSB equilibrium concentrations in the specified environment.

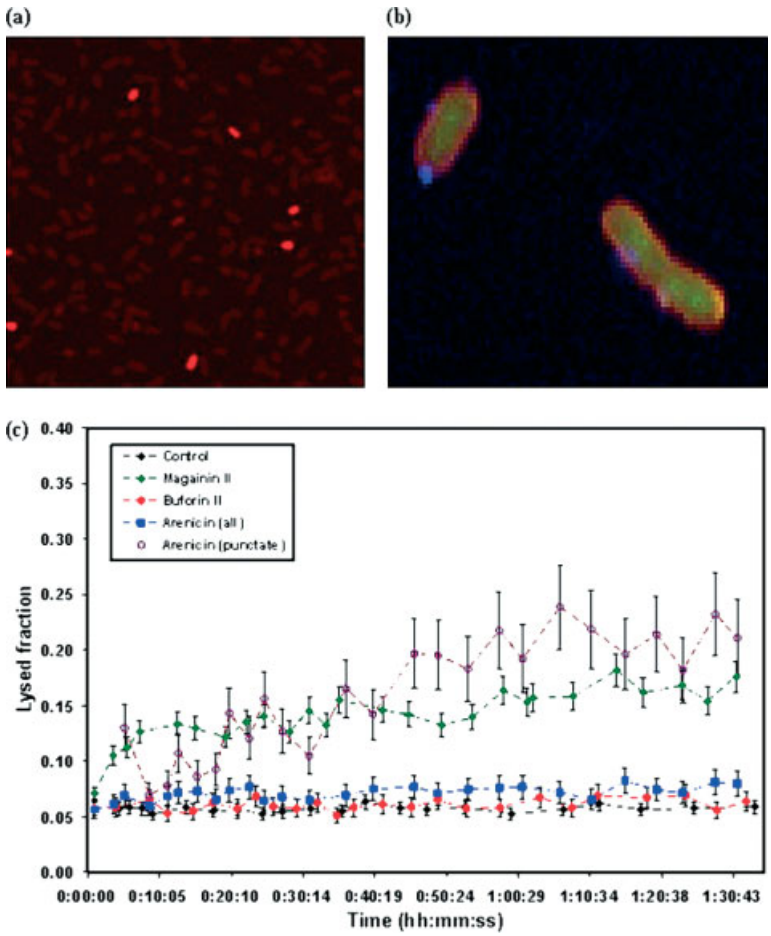

Figure 5. Lysis of *E. coli* by AMPs. (a) Low magnification fluorescence image (20×) of log phase, untreated *E. coli* exposed to PI: dim bacteria are alive and bright bacteria are dead. (b) High magnification hyperspectral image of arenicin aggregates (blue) interacting with log-phase *E. coli* exposed to PI (membrane component = red, cytosolic component = yellow-green). (c) Time course of *E. coli* lysis rate following exposure to each AMP as indicated by fraction of cells with PI signals in excess of 3× of the average PI signal.

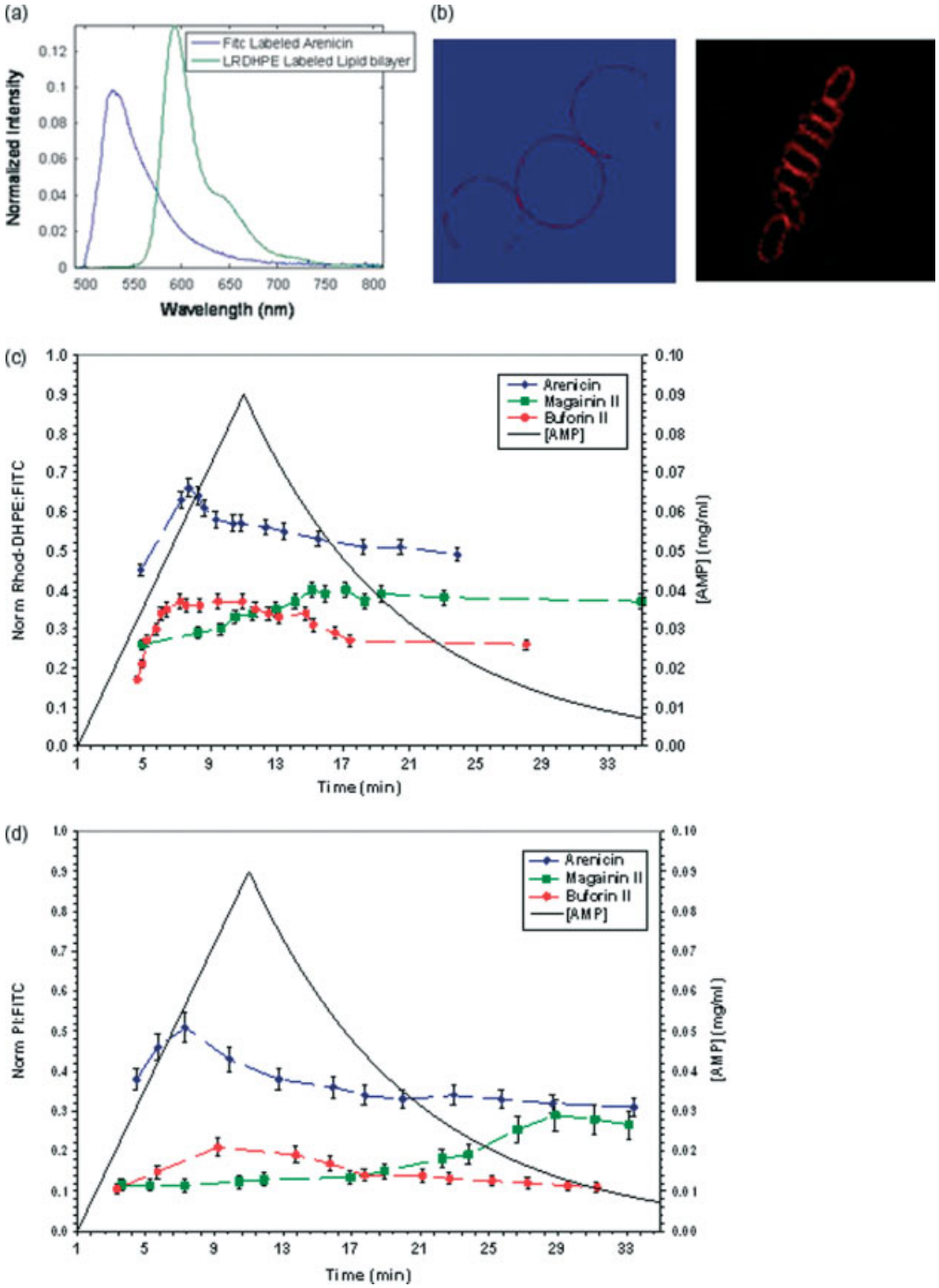

Figure 6. Temporal FRET interaction between the AMPs and membrane in a flow cell, measured by the ratio of MCR generated spectral component intensities in membrane mask pixels of the image. (a) Representative emission spectra of the fluorescent AMP conjugates and the SB cell membrane; (b) membrane masks of SBSBs and *E. coli*, respectively; (c) time series FRET signal from SBSBs, normalized to the membrane acceptor (rhod-DHPE) emission prior to exposure to AMP; and (d) time series FRET signal from *E. coli*, normalized to the membrane acceptor (PI) emission prior to exposure to AMP.

10 min pulse of 0.1 mg/ml fluorescent AMP solution, followed by flushing the system with 1× PBS for the remainder of the assay. During the exposure, confocal spectral images were collected at regular intervals and the images were analyzed using MCR. FRET analysis was then performed by masking the membrane regions and finding the average ratio of Rhod-DHPE membrane acceptor to FITC-AMP donor intensities.

Corresponding time series FRET measurements were performed for monitoring AMP interactions with the *E. coli* outer membrane. This was accomplished by briefly equilibrating a log-phase LB media suspended culture aliquot containing 0.125 mg/ml PI in 1× PBS, introducing a 10 min pulse of 0.1 mg/ml fluorescent AMP solution, and flushing the system with 1× PBS for the remainder of the assay. Confocal spectral images for MCR and subsequent FRET analysis were collected at regular intervals throughout this procedure. FRET analysis was performed as above, with masking of the membrane regions and finding the average ratio of PI membrane acceptor to FITC-AMP donor intensities.

Journal of PeptideScience

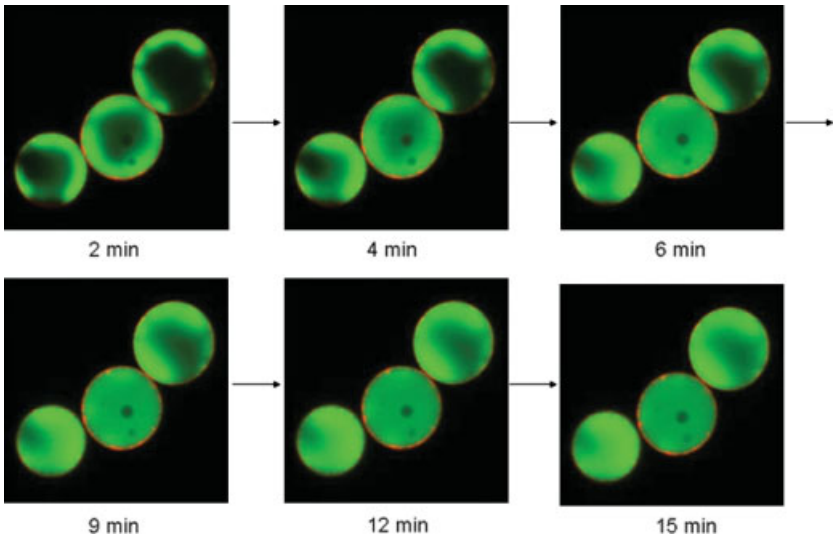

Figure 7. Flow cell time course of FITC-buforin II (green) breach of the SBSBs (red), and adsorption to the nanoporous silica matrix. Note in the 2 min time slice that the areas of the beads that are breached more quickly correspond to the outer surfaces of the SBSBs where FRET, and therefore AMP-membrane interaction, is the greatest (see Figure 6b with FRET masks outlined for these same SBSBs).

In comparing the FRET results with SBSBs and *E. coli*, similar trends in the overall dynamics are observed; however, discrepancies in the binding intensities and kinetics are also observed. In order to directly compare the binding intensities and kinetics from the FRET results, the relative spectral overlap between the emission of FITC-AMP and the absorption of Rhod-DHPE and PI were calculated in concentration-matched controls with 488 nm excitation. Specifically, this calculation was performed by finding the ratio of the integrated spectral overlap between the MCR generated Rhod-DHPE spectrum and each of the concentration-matched fluorescence acceptor spectra. The results of this calculation suggest that the membrane component of PI has spectral overlap with FITC-AMP that is 81% of the spectral overlap between FITC-AMP and Rhod-DHPE. Using this correction, the maximum FRET ratios observed between the AMPs and the PI outer membrane label in *E. coli* were approximately equal to the model system with magainin II and arenicin, but only 80% of the model system with buforin II. Comparison of the FRET kinetics of the membrane interactions between *E. coli* and SBSBs exhibit more significant differences. In the case of magainin II, although similar immediate associations are observed, the grow-in of the highest intensity membrane-bound state(s) in *E. coli* is not observed until ~17 min after the flow of the AMP is stopped, whereas this is observed at ~4 min in the model system. For buforin II, accumulation in the bacterial membrane is slower, peaking ~2 min after the model system, with the binding plateau and release occurring on a similar, but slower time scale. We suggest that both results can be ascribed in various degrees to the availability of the additional membrane components of the *E. coli* cellular envelope into which the AMPs partition. For arenicin, the large initial association with the membrane is nearly identical to the model system, but the peak occurs in *E. coli* faster than in the model system by ~1 min with a very similar decay, suggesting the possibility of high outer membrane-specific activity of this peptide.

Membrane breach

In the experiments with SBSBs, all arenicin that entered the bilayer was retained, whereas with magainin II and buforin II, the membrane was breached and the AMP adsorbed to the nanoporous silica matrix encapsulated by the supported bilayer, as shown in Figure 7. This observation is consistent with the observed FRET kinetics of buforin II, where there is an initial increase in bilayer-AMP association, which then decreases. Although magainin II also breaches the supported bilayer, there is no evidence of decrease in the FRET signal over the course of the time series. This observation highlights the mechanistic differences of membrane translocation between buforin and magainin. One possible interpretation of this result is that as magainin accumulates in the membrane, transport of additional peptides through the membrane is facilitated. In the case of arenicin, there is an initial increase in interactions with the supported bilayer, followed by a decrease. When combined with the fact that arenicin does not breach the membrane, this is suggestive of either structural rearrangement of the peptide, which shields or quenches the N-terminal fluorescent conjugate or the formation of a multimeric state that excludes direct interactions of peptide monomers with the membrane. It is also important to note that although arenicin is a cationic peptide, like magainin II and buforin II, it is unlike the others in that arenicin's interactions with the bilayer greatly exceed the electrostatic attraction of the silica matrix. This result is especially relevant in showcasing the gross effects of physiologically dependent peptide folding distortions of bulk properties, which would otherwise be homogenous among these peptides.

Discussion

In order to generate a reductionist system for which to compare data collected on living bacteria, the previously described supported bilayer system [45,46], which employed phosphocholine (PC) membranes for ion and fluorophore release assays, was modified to mimic membranes present in bacterial systems. To mimic the charge and common constituents of typical bacterial inner membranes, the bacterial phospholipids *E. coli* PG and *E. coli* PE were employed in equal molar ratios. Unlike zwitterionic PC membranes, however, anionic liposomes are electrostatically inhibited

from supported bilayer formation on the mutually anionic silica particles. This was overcome by introducing Ca^{2+} to the buffer used during supported bilayer formation. Using bulk fluorescence assays and fluorescence spectral imaging, we observed that between 5 and 10 mM Ca^{2+} ion produces consistent multilamellar supported bilayers, which can be delaminated down to a single supported bilayer within six wash cycles with low ionic strength buffer. Although the complexity intrinsic to even a simple bacterial cellular envelope is impossible to produce synthetically, the PE/PG bilayer membrane provides a simple model for the largely homogenous and symmetric inner membrane in solubility, thickness, and electrostatics [47]. Other minimal components that must be considered are the mesh-like peptidoglycan layer, periplasmic spaces, and structural proteins in gram-positive bacteria; and the additional asymmetric outer membrane of gram-negative bacteria [48].

In addition to studies of model membrane systems, hyperspectral fluorescence images can provide further understanding of the interaction of AMPs with both model membrane systems and actual bacterial systems. MCR is a powerful technique for data analysis of the hyperspectral fluorescence images of these biologically representative systems because it can provide quantitative analysis of the image data without the need for standards and can discover all the emitting species present in an image, even those about which there is no *a priori* information. A primary research advantage of hyperspectral imaging with the use of MCR algorithms is that it allows separation of many overlapping fluorophores and thus generates quantitatively interpretable images without cross talk between fluorophores [28,49]. In order to leverage and extend these capabilities, much of the experimental work presented here was aimed at developing comparative interfaces between the biological systems under investigation and the existing optical infrastructure. These interfaces consisted of fluorescence labeling schemes, sample and flow cells, time series imaging with confocal sectioning modalities, and spectral image processing with our fast, robust MCR algorithms.

Of particular interest during hyperspectral imaging was the capability of tracking the time course of interactions of various AMPs with model and bacterial membranes and comparing these interactions with non-membrane localized activity. In order to realize this goal, several membrane and cytosolic fluorescence labeling schemes were developed and compared. For monitoring AMP localization in SBSBs, Rhod-DHPE was introduced in the starting phospholipid solution and was found to produce stable and uniformly labeled supported bilayers at mole fractions of 1% mol/mol. For monitoring AMP localization in *E. coli,* several labeling methods were found to be unsatisfactory, including covalent fluorescence modification of nonspecific membrane proteins, fluorescence exchange between liposomes and micelles, and electrostatic fluorescence binding. However, using the high spectral resolution of the confocal fluorescence spectral microscope coupled with MCR analysis demonstrated that PI, a commonly used intensity-based indicator of cell lysis [37], exhibits a ~10 nm fluorescence red-shift when partitioned in the LPS-containing gram-negative outer membrane relative to the peak fluorescence emission of PI in the cytoplasm. With the use of MCR, these two PI fluorescence components were spectrally and spatially separated, allowing unambiguous demarcation of the *E. coli* cellular envelope and subsequent FRET analysis.

Parallel comparison of the interaction dynamics and equilibria of AMPs with SBSBs and *E. coli* provides a unique perspective that can be used for both peptide characterization and assessment of biomimetic systems for biomedical research. Several important insights were gained by comparing the supported bilayer and bacterial interactions of the AMP, arenicin to that of two well-studied examples: magainin II and buforin II. First, like magainin II, arenicin results in membrane disruption leading to lysis and bacterial death, although multimeric aggregation of arenicin appears to play an important role in this process, suggestive of a carpet model-like membrane disruption mechanism [4,50]. FRET data, which provided sub-diffraction limited spatial resolution of membrane–AMP binding interactions, suggest that diverse time-dependent mechanisms exist among the three AMPs. Consistent with other previously cited studies, buforin II appears to accumulate in the membrane to some degree, followed by membrane penetration without permeabilization. In the case of magainin II, combining the FRET results and the observation of membrane breach suggest that the AMP accumulates in the membrane, facilitating the passage of additional peptides through the membrane and into the internal cellular matrix. This result is consistent with previous work which suggests that magainin II forms multimeric channel structures characterized by large pore diameters and strong interactions with phospholipid components of the membrane [14]. Although somewhat similar to magainin II, arenicin shows an even higher degree of initial accumulation in the membrane, accompanied by the formation of heterogeneous multimeric aggregates [51]. It is important to note, however, that in all cases, the AMPs were observed in significant concentrations in the cytosolic region of *E. coli*, suggesting the possibility of additional membrane penetration enabled bacteriocidal activity like those observed previously with buforin II [52].

Conclusion

Several important observations were made in comparing the interactions of buforin II, magainin II, and arenicin with SBSBs and *E. coli*. These observations were derived from three primary categories of experimental approaches and data: (i) fluorescence imaging to obtain a direct comparison of model and living systems; (ii) the experimental measurement of comparative local equilibrium concentrations of the different antimicrobial agents' partitioning in the described systems; and (iii) collection of data leading to a deeper understanding of the roles of membrane penetration and permeabilization in the action of AMPs.

Interfacing hyperspectral confocal microscopy with MCR was key to solving several challenges in this effort. For example, using the high spectral resolution of the confocal hyperspectral microscope with the spectral separation and quantitative capabilities of MCR spectral image analysis allowed the discovery of a unique environmental sensitivity property of a commonly used cell death indicator, PI, which was then applied as a membrane label and FRET acceptor in multiple comparative studies.

The observation of membrane breach of magainin II and buforin II into the nanoporous silica matrix of SBSBs is consistent with multiple reports in the literature of interactions with these AMPs and living systems [4,5,17,18,53]. The additional similarities between the membrane interactions of the model and living system identified using time series FRET yield further confidence in the importance of reductionist reference systems for understanding the biophysics of molecular interactions usually found in more complicated environments. However, discrepancies in membrane-binding intensities and kinetics, and the disagreement of the local equilibrium concentrations of arenicin between the

Journal of PeptideScience

model system and *E. coli* suggest several difficulties in general application of such model systems for therapeutic development efforts. To address these difficulties, future work in this area will require rational biomimetic modification of the silica substrate to minimize the perturbations observed. Several strategies have been described to minimize these unnatural and sometimes denaturing effects [54–56] and should be amenable to the encapsulation strategies described in this work. For other applications, however, the observation of adsorption of buforin II and magainin II to the internal silica matrix may serve as an important example of a method of controlled release of AMPs for integrated microbial control applications [57].

Acknowledgements

We specially thank Rand Garfield (Sandia National Labs) for his work in developing the sample flow cell for use with the 3D Hyperspectral Imager. We would also like to thank Mike Keenan (Sandia National Labs) for software development efforts and high speed MCR algorithms. Finally, we would also like to thank Heather Luckarift and Glenn Johnson of the Air Force Research Laboratory (Tyndall Air Force Base, FL, USA) for their helpful discussions involving their observations of AMP interactions with silica substrates. Sandia is a multi-program laboratory operated by Sandia Corporation, a Lockheed Martin Company, for the United States Department of Energy under Contract DE-ACO4-94AL85000.

Supporting information

Supporting information may be found in the online version of this article.

References

1 Canon M. A family of wound healers. *Nature* 1987; **328**: 478.
2 Zasloff M. Antimicrobial peptides of multicellular organisms. *Nature* 2002; **415**: 389–395.
3 Giacometti A, Cirioni O, Del Prete MS, Barchiesi F, Paggi AM, Petrelli E, Scalise G. Comparative activities of polycatioinic peptides and clinically used antimicrobial agents against multidrug-resistant nosocomial isolates of *Acinetobacter baumannii*. *J. Antimicrob. Chemother.* 2000; **46**: 807–810.
4 Shai Y, Oren Z. From "carpet" mechanism to de-novo designed diasteriomeric cell-selective antimicrobial peptides. *Peptides* 2001; **22**: 1629–1641.
5 Bowman HG. Anitbacterial peptides: basic facts and emerging concepts. *J. Intern. Med.* 2003; **254**: 197–215.
6 Westerhoff HV, Zasloff M, Rosner JL, Hendler RW, De Waal A, Vaz Gomes A, Jongsma PM, Riethorst A, Juretic D. Functional synergism of the magainins PGLa and magainin-2 in *Esherichia coli*, tumor cells and liposomes. *Eur. J. Biochem.* 1995; **228**: 257–264.
7 Giacometti A, Cirioni O, Barchiesi F, Fortuna M, Scalise G. In-vitro activity of cationic peptides alone and in combination with clinically used antimicrobial agents against *Pseudomonas aeruginosa*. *J. Antimicrob. Chemother.* 1999; **44**: 641–645.
8 Cruz-Chamorro L, Puertollano MA, Puertollano E, de Cienfuegos GA, de Pablo MA. In vitro biological activities of magainin alone or in combination with nisin. *Peptides* 2006; **27**: 1201–1209.
9 Yount NY, Yeaman MR. Multidimensional signatures in antimicrobial peptides. *Proc. Natl. Acad. Sci. U.S.A.* 2004; **101**: 7363–7368.
10 Fjell CD, Hancock REW, Cherkasov A. AMPer: a database and an automated discovery tool for antimicrobial peptides. *Bioinformatics* 2007; **23**: 1148–1155.
11 Guiliani A, Pirri G, Nicoletto SF. Antimicrobial peptides: an overview of a promising class of therapeutics. *Cent. Eur. J. Biol.* 2007; **2**: 1–33.
12 Zasloff M. Magainins, a class of antimicrobial peptides from *Xenopus* skin: Isolation, characterization of two active forms, and partial c-DNA sequence of a precursor. *Proc. Natl. Acad. Sci. U.S.A.* 1987; **84**: 5449–5453.
13 Duclohier H, Molle G, Spach G. Antimicrobial peptide magainin I from Xenopus skin forms anion-permeable channels in planar lipid bilayers. *Biophys. J.* 1989; **56**: 1017–1021.
14 Matsuzaki K, Murase O, Fujii N, Miyajima K. Translocation of a channel-forming antimicrobial peptide, magainin 2, across lipid bilayers by forming a pore. *Biochemistry* 1995; **34**: 6521–6526.
15 Hara T, Kodama H, Kondo M, Wakamatsu K, Takeda A, Tachi T, Matsuzaki K. Effects of peptide dimerization on pore formation: Antiparallel disulfide-dimerized magainin 2 analogue. *Biopolymers* 2001; **58**: 437–446.
16 Park CB, Kim HS, Kim SC. Mechanism of action of the antimicrobial peptide buforin II: buforin II kills microorganisms by penetrating the cell membrane and inhibiting cellular functions. *Biochem. Biophys. Res. Commun.* 1998; **244**: 253–257.
17 Takeshima K, Chikushi A, Lee K-K, Yonehara S, Matsuzaki K. Translocation of analogues of the antimicrobial peptides magainin and buforin across human cell membranes. *J. Biol. Chem.* 2003; **278**: 1310–1315.
18 Kobayashi S, Chikushi A, Tougu S, Imura Y, Nishida M, Yano Y, Matsuzaki K. Membrane translocation mechanism of the antimicrobial peptide buforin 2. *Biochemistry* 2004; **43**: 15610–15616.
19 Uyterhoeven ET, Butler CH, Ko D, Elmore DE. Investigating the nucleic acid interactions and antimicrobial mechanism of buforin II. *FEBS Lett.* 2008; **582**: 1715–1718.
20 Yi GS, Park CB, Kim SC, Cheong C. Solution structure of an antimicrobial peptide buforin II. *FEBS Lett.* 1996; **398**: 87–90.
21 Park CB, Yi K-S, Matzusaki K, Kim MS, Kim SC. Structure-activity analysis of buforin II, a histone H2A-derived antimicrobial peptide: the proline hinge is responsible for the cell penetrating ability of buforin II. *Proc. Natl. Acad. Sci. U.S.A.* 2000; **97**: 8245–8250.
22 Ovchinnikova TV, Aleshina GM, Baladin SV, Krasnosdembskaya AD, Markelov ML, Frovolova EI, Leonova YF, Tagaev AA, Krasnodembsky EG, Kokryakov VN. Purification and primary structure of two isoforms of arenicin, a novel antimicrobial peptide from marine polychaeta *Arenicola marina*. *FEBS Lett.* 2004; **577**: 209–214.
23 Lee J-U, Kang D-I, Zhu WL, Shin SY, Hahm K-S, Kim Y. Solution structures and biological functions of the antimicrobial peptide, arenicin-1, and its linear derivative. *Pept. Sci.* 2007; **88**: 208–216.
24 Ovchinnikova TV, Shenkarev ZO, Balandin SV, Nadezhin KD, Paramonov AS, Kokryakov VN, Arseniev AS. Molecular insight into the mechanism of antimicrobial action of the ß-hairpin peptide arenicin: specific oligomerization in detergent micelles. *Biopolymers* 2007; **89**: 455–464.
25 Andrä J, Jakovkin I, Grötzinger J, Hecht O, Krasnosdembskaya A, Goldmann T, Gutsmann T, Leippe M. Structure and mode of action of the antimicrobial peptide arenicin. *Biochem. J.* 2008; **410**: 113–122.
26 Bradburne JA, Godfry P, Choi JH, Mathis JN. In vivo labeling of *Escherichia coli* cell envelope proteins with N-hydroxysuccinimide esters of biotin. *Appl. Environ. Microbiol.* 1993; **59**: 663–668.
27 Sinclair MB, Haaland DM, Timlin JA, Jones HDT. Hyperspectral confocal microscope. *Appl. Opt.* 2006; **45**: 6283–6291.
28 Haaland DM, Jones HDT, Sinclair MB, Carson B, Branda C, Poschet JF, Rebeil R, Tian B, Liu P, Brasier AR. Next-generation spectroscopic technologies. Proceedings of SPIE, 6765 SPIE: Boston, MA, 2007.
29 Van Benthem MH, Keenan MR, Haaland DM. Application of equality constraints on variables during alternating least squares procedures. *J. Chemometr.* 2002; **16**: 613–622.
30 Van Benthem MH, Keenan MR. Fast algorithm for the solution of large-scale non-negativity-constrained least squares problems. *J. Chemometr.* 2004; **18**: 441–450.
31 Tauler R, Casassas E, Izquierdoridorsa A. Self-modeling curve resolution in studies of spectrometric titrations of multi-equilibria systems by factor-analysis. *Anal. Chim. Acta* 1991; **248**: 447–458.
32 de Juan A, Tauler R. Multivariate curve resolution (MCR) from 2000: progress in concepts and applications. *Crit. Rev. Anal. Chem.* 2006; **36**: 163–176.
33 Kotula PG, Keenan MR, Michael JR. Automated analysis of SEM X-ray spectral images: a powerful new microanalysis tool. *Microsc. Microanal.* 2003; **9**: 1–17.

34 Ohlhausen JAT, Keenan MR, Kotula PG, Peebles DE. Multivariate statistical analysis of time-of-flight secondary ions mass spectrometry images using AXSIA. *Appl. Surf. Sci.* 2004; **231/232**: 230–234.
35 Keenan MR, Kotula PG. Accounting for Poisson noise in the multivariate analysis of ToF-SIMS spectrum images. *Surf. Interface Anal.* 2004; **36**: 203–212.
36 Jones HDT, Haaland DM, Sinclair MB, Melgaard DK, Van Benthem MH, Pedroso MC. Weighting hyperspectral image data for improved multivariate curve resolution results. *J. Chemometr.* 2008; **22**: 482–490.
37 Banning N, Toze S, Mee BJ. *Escherichia coli* survival in groundwater and effluent measured using a combination of propidium iodide and the green fluorescent protein. *J. Appl. Microbiol.* 2002; **93**: 69–76.
38 Chopra I. The magainins: antimicrobial peptides with potential for topical application. *J. Antimicrob. Chemother.* 1993; **32**: 351–353.
39 Rausch JM, Marks JR, Wimley WC. Rational combinatorial design of pore-forming ß-sheet peptides. *Proc. Natl. Acad. Sci. U.S.A.* 2005; **102**: 10511–10515.
40 Yang L, Gordon VD, Mishra A, Som A, Purdy KR, Davis MA, Tew GN, Wong GCL. Synthetic antimicrobial oligomers induce a composition-dependent topological transition in membranes. *J. Am. Chem. Soc.* 2007; **129**: 12141–12147.
41 Glukhov E, Burrows LL, Deber CM. Membrane interactions of designed cationic antimicrobial peptides: two thresholds. *Biopolymers* 2008; **89**: 360–371.
42 Bechinger B, Lohner K. Detergent-like actions of linear amphipathic cationic antimicrobial peptides. *Biochim. Biophys. Acta* 2006; **1758**: 1529–1539.
43 Jones G, Vullev VI II. Medium effects on the photophysical properties of terbium(III) complexes with pyridine-2,6-dicarboxylate. *Photochem. Photobiol. Sci.* 2002; **1**: 925–933.
44 Lakowicz JR. *Principles of Fluorescence Spectroscopy*, 2nd edn. Kluwer Academic/Plenum Publishers: New York, 1999.
45 Davis RW, Flores A, Barrick TA, Cox JM, Brozik SM, Lopez GP, Brozik JA. Nanoporous microbead supported bilayers: Stability, physical characterization, and incorporation of functional transmembrane proteins. *Langmuir* 2007; **23**: 3864–3872.
46 Burunda T, Huang J, Ramarao GV, Ista LK, Larson RS, Ward TL, Sklar LA, Lopez GP. Biomimetic molecular assemblies on glass and mesoporous silica microbeads for biotechnology. *Langmuir* 2003; **19**: 1654–1663.
47 Leive L. *Bacterial Membranes and Walls*. M. Dekker: New York, 1973.
48 Cevc G, Marsh D. *Phospholipid Bilayers*. Wiley and Sons: New York, 1987.
49 Vermaas WFJ, Timlin JA, Jones HDT, Sinclair MB, Nieman LT, Hamad SW, Melgaard DK, Haaland DM. In vivo hyperspectral confocal fluorescence imaging to determine pigment localization and distribution in cyanobacterial cells. *Proc. Natl. Acad. Sci. U.S.A.* 2008; **105**: 4050–4055.
50 Shai Y. Molecular recognition between membrane spanning polypeptides. *Trends Biochem. Sci.* 1995; **20**: 460–464.
51 Arnusch CJ, Branderhorst H, de Kruijff B, Liskamp RM, Breukink E, Pieters RJ. Enhanced membrane pore formation by multimeric/oligomeric antimicrobial peptides. *Biochemistry* 2007; **46**: 13437–13442.
52 Brogden KA. Antimicrobial peptides: pore formers or metabolic inhibitors in bacteria?. *Nat. Rev. Microbiol.* 2005; **3**: 238–250.
53 Henriques ST, Melo MN, Castanho MARB. Cell-penetrating peptides and antimicrobial peptides: how different are they?. *Biochem. J.* 2006; **399**: 1–7.
54 Castellana ET, Cremer PS. Solid supported lipid bilayers: from biophysical studies to sensor design. *Surf. Sci. Rep.* 2006; **61**: 429–444.
55 Merzlyakov M, Li E, Gitsov I, Hristova K. Surface-supported bilayers with transmembrane proteins: role of the polymer cushion revisited. *Langmuir* 2006; **22**: 10145–10151.
56 Wagner ML, Tamm LK. Tethered polymer-supported planar lipid bilayers for reconstitution of integral membrane proteins: silane-polyethyleneglycol-lipid as a cushion and covalent linker. *Biophys. J.* 2000; **79**: 1400–1414.
57 Eby DM, Farrington KE, Johnson GR. Synthesis of bioinorganic antimicrobial peptide nanoparticles with potential therapeutic properties. *Biomacromolecules* 2008; **9**: 2487–2494.

